Available online at www.sciencedirect.com
SCIENCE DIRECT®
Journal of Electron Spectroscopy and Related Phenomena 141 (2004) 229–238
JOURNAL OF ELECTRON SPECTROSCOPY and Related Phenomena
www.elsevier.com/locate/elspec

Multicoincidence studies of photo and Auger electrons from fixed-in-space molecules using the COLTRIMS technique

T. Jahnke[a], Th. Weber[a], T. Osipov[b], A.L. Landers[c], O. Jagutzki[a], L.Ph.H. Schmidt[a], C.L. Cocke[d], M.H. Prior[b], H.Schmidt-Böcking[a], R.Dörner[a]*

[a] *Institut für Kernphysik, University of Frankfurt, August-Euler Str 6, D-60486 Frankfurt, Germany*
[b] *Lawrence Berkeley National Laboratory, Berkeley, CA 94720, USA*
[c] *Physics Department, Auburn University, Auburn, AL 36849, USA*
[d] *Department of Physics, Kansas State University, Cardwell Hall, Manhattan, KS 66506, USA*

Received 23 April 2004; received in revised form 23 June 2004; accepted 24 June 2004
Available online 16 September 2004

Abstract

This report will introduce the reader to the method of measuring electron and ion momentum distributions from fixed-in-space molecules using modified versions of the COLTRIMS technique. Following the introduction and a description of the working principles of this technique, a detailed discussion of the design of the electron and the ion detection part of the spectrometer will be presented. The actual measurement represents only a minor fraction of a COLTRIMS-like experiment. We therefore give an in-depth view at the basics of the offline-analysis for the field of detecting multiple particles from a Coulomb exploding molecule. Achievable resolutions, the possibilities of background suppression via multiparticle software coincidence methods, and the improvement of electron momentum resolution by center-of-mass-correction will be discussed, followed by an example of a setup for low energy electrons (<10 eV).

Apart from the introduction to the treatment of the acquired data, a recent development on the hardware of the spectrometer will be presented. We have for the first time used a retarding field in the spectrometer's electron arm. This provides the possibility of measuring high energy Auger electrons of ∼300 eV. A typical implementation for an experiment on Auger electrons from fixed-in-space nitrogen will be shown.

The article will close with examples of recent measurements of photoionization of fixed-in-space carbon monoxide.

Keywords: Photoionization; Fixed-in-space molecules; Hardware

1. Introduction

Within the dipole approximation the angular distribution of photoelectrons emitted from an ensemble of unaligned atoms by linearly polarized light into a solid angle element at angle θ with respect to the polarization is described by one free parameter, β (1):

$$\frac{\partial\sigma}{\partial\Omega} = \frac{\sigma}{4\pi}\left(1 + \frac{\beta}{2}(3 \times \cos^2\theta - 1)\right), \quad (1)$$

where σ is the total photoionization cross-section at the particular photon energy. In (1), β multiplies the second Legendre-polynomial, reflecting the fact that the maximum amount of angular momentum transferable by a photon is $1\hbar$. This description does not change when photoelectrons are observed from randomly aligned molecules. If, however, the molecule is aligned, or "fixed-in-space", with respect to the light's polarization, the photoelectron's angular distribution may show rich structures from contributions of angular momenta higher than $1\hbar$. This is possible as only the sum of the angular momentum transferred to the electron and the ionized molecule must equal $1\hbar$. The angular momentum parts of the continuum electron and the molecular ion wavefunctions are mirror images of each other. The electron leaves behind a molecular ion rotational wave packet, which is a coherent superposition of many angular momentum states (2). Correspondingly, the continuum electron wave is a superposi-

* Corresponding author.
E-mail address: doerner@hsb.uni-frankfurt.de (R. Dörner).

0368-2048/$ – see front matter © 2004 Published by Elsevier B.V.
doi:10.1016/j.elspec.2004.06.010

tion of many angular momentum components. This angular momentum coherence between electron and molecular ion results from the multiple scattering of the electron wave as it emerges through the molecular potential. This leads to measurable contributions of even $l = 5$ to the molecular frame K-photoelectron angular distribution of carbon monoxide (3–8) (see also e.g. (9–15)). The view that the electron emission structure is the diffraction pattern of an electron wave launched within the molecular potential has been suggested as perhaps being a more descriptive explanation. Patterns of electron emissions from fixed-in-space molecules may therefore be understood as the result of illuminating the molecule from within (3) using an electron wave; such patterns are sensitive probes of the molecular potential (16). Similar X-ray photoelectron diffraction (XPD) techniques have previously been possible only in crystals (17) and absorbates (18), where they have provided information on physical properties such as the positions of nearest neighbors.

Experimentally, in order to achieve the spatial alignment of molecules electric fields have been used. These may arise from intense laser pulses (19), or DC fields from multipole electric structures acting on molecular beams (see e.g. (20)), or from the environment on a surface (21). The latter approach has the complication (or the richness) of the interaction of the sample molecule and the emerging electron with the surface. More recently, studies of fixed-in-space molecules in the gas phase have been performed (3–7,9–16,22–25), where the molecule is not fixed in the laboratory frame, but rather its spatial alignment during photoionization is inferred from its fragment momenta measured in coincidence with the photoelectron.

This method is applicable to molecules with certain, but fairly common properties. (i) To measure the direction of the molecular axis, the molecule must fragment into at least one ionized part emitted along that axis. The measured momentum (or even only the direction of emission) of the fragment then gives the molecule's orientation; (ii) to reflect the orientation at the time of photoionization the time between photoionization and dissociation must be short compared to the rotational period of the molecule; this is the often quoted "Axial Recoil Approximation" (7,26). In all of the examples included here the diatomic molecule dissociates into two ion fragments. Measuring momentum of each fragment has some advantages that will be described. A typical experiment will accumulate coincident momentum measurements of the electrons and ion fragments from hundreds of thousands or even millions of ionization events. These are sorted and plotted in the form of various kinds of histograms; in particular the electron momenta are easily transformed into the molecular frame, the result being the same as if the molecule had been fixed-in-space in the laboratory.

During the last 4 years a modified version of the well established COLd Target Recoil Ion Momentum Spectroscopy (COLTRIMS) (see (27,28) for recent reviews) has been applied successfully to investigate photo (3,4,7,25,29) and Auger electrons (30,31) from fixed-in-space molecules. In this approach a supersonic gas jet is crossed with a photon beam forming a well defined reaction volume (roughly a 1 mm cube). When a photoionization event occurs, the ionic and electronic fragments are guided to two position sensitive detectors by an electric field. A superimposed homogeneous magnetic field radially confines electrons up to a certain energy inside the spectrometer's volume (see Fig. 1) (32). By recording the times of flight and the positions of impact on the detectors, the initial vector momenta can be reconstructed during offline analysis. Fortunately this approach often can achieve 4π solid angle collection efficiency for all the photo fragments.

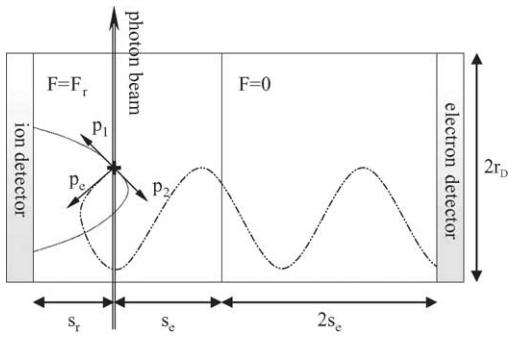

Fig. 1. A typical COLTRIMS spectrometer employing Wiley–McLaren time focusing on the electron side. The supersonic gas jet, coming out of the picture plane, is crossed with the photon beam at the marked spot. The molecular photo fragments are accelerated toward their detectors by the uniform electric field F_r that extends over lengths s_r to the ion detector and s_e toward the electron detector. Following acceleration the electrons move through the electric field free drift region of length $2s_e$ The electrons perform a cyclotron motion due to the superimposed uniform magnetic field along the z-axis.

In the following we will describe the spectrometer design and the procedure of data analysis for the ion side, for low energy electrons (<100 eV) and for electrons of high energy (> 100 eV).

2. Ion spectrometer arm

Inner shell photoionization of a diatomic molecule is a typical example where this approach has been used. In most cases a second electron is emitted by the Auger process following emission of the photo electron. This yields a doubly (or more) charged molecular ion that rapidly fragments. The energy of the molecule's ionic fragments is typically in the range of several electron volts (eV) (i.e. the Coulomb potential energy of the ions at their initial internuclear separation).

The design of the ion-side of the spectrometer is largely determined by the energies and masses of the ion fragments to be detected. As the size of the position sensitive detector is limited, the acceleration length of the ion-side and the spectrometer's electric field are chosen such that ion pairs with the highest energy to be detected hit the detector's active area regardless of their orientation (if 4π collection efficiency is to be achieved). The relationship between electric field F_r and

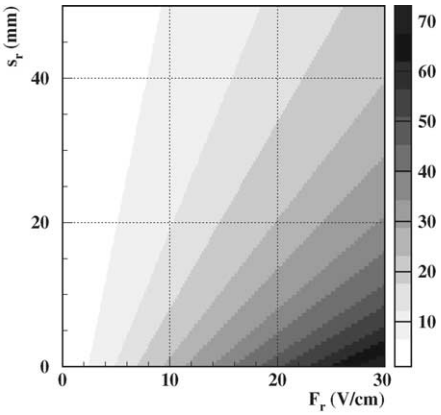

Fig. 2. Maximum ion energy in eV (gray value) that can be detected with a detector of 80 mm diameter employing an electric field of F_r and a ion spectrometer length of s_r.

distance from the interaction volume to the detector s_r for a range of ion energies E_{ion} is shown in Fig. 2 for a 80 mm detector. The momentum measurements associated with these experiments are derived from measurements of particle positions and flight times. The latter are measured with respect to the pulsed ionizing radiation, usually from an electron synchrotron. (The LBNL Advanced Light Source, operating in two-bunch mode, produces roughly 30 ps wide x-ray pulses separated by 328 ns.) All times are measured with respect to a marker pulse synchronized to the x-ray pulses. In the laboratory frame the momentum of ion i with mass m_i and charge q_i is therefore given by:

$$p_{i,x} = \frac{m_i(x_i - x_{orig})}{t_i} \tag{2}$$

$$p_{i,y} = \frac{m_i(y_i - y_{orig})}{t_i} - v_{jet}m_i \tag{3}$$

$$p_{i,z} = \frac{s_r m_i}{t_i} - \frac{F_r q_i t_i}{2} \tag{4}$$

Here (x_i, y_i) are the measured positions of impact of an ionic fragment i on the detector. The coordinates of the starting point of the trajectory (x_{orig}, y_{orig}) are in general only known with a precision given by the size of the interaction volume. Therefore the size of the gas jet and the beam focus in general limit the momentum resolution.

The equation for the momentum in y-direction reflects the fact that this direction is defined to be the direction of the supersonic jet. The jet is internally cold but its particles have a directed motion with a mean velocity v_{jet}. Because the spread relative to the mean jet velocity is small and, as the jet velocity is known to be $v_{jet} = \sqrt{7kT_0/M}$ (with the initial temperature of the gas T_0 in K and the molecular mass M), the momentum associated with the motion of the jet is subtracted.

For a diatomic where both fragments are detected, the resolution on the relative energy (KER) of the ionic fragments is greatly enhanced. By making use of momentum conservation and calculating the relative momentum with respect to the center of mass, the initial starting point (x_{orig}, y_{orig}) of the measured particles can actually be canceled out. This is of great advantage as the uncertainty introduced to the measurement due to the spread of the target zone is a major source for resolution broadening on the ion momenta. Therefore, a gain in energy resolution of a factor of ~10 is achievable. For the case of the center-of-mass momentum being zero, apart from the momentum introduced from the jet velocity, the equation for $\vec{p}_{rel,}$ is found to be:

$$\vec{p}_{rel,} = \vec{p}_1 = -\vec{p}_2 \tag{5}$$

This leads, for the x and y directions, to a form that depends on the difference of the measured positions of impact of the two ions, i.e. $(x_1 - x_2)$ and $(y_1 - y_2)$, and therefore is independent of (x_{orig}, y_{orig}):

$$p_{rel,x} = m_1 m_2 \frac{x_1 - x_2}{t_2 m_1 + t_1 m_2} \tag{6}$$

$$p_{rel,y} = m_1 m_2 \frac{(y_1 - y_2) + v_{jet}(t_2 - t_1)}{t_2 m_1 + t_1 m_2} \tag{7}$$

$$p_{rel,z} = \frac{E}{2}\left(\frac{t_2^2 q_2 m1 - t_1^2 q_1 m_2}{t_1 m_2 + t_2 m_1}\right) \tag{8}$$

The kinetic energy release (KER), i.e. the sum energy of the ionic fragments obtained from the coulomb explosion, are given from the relative momenta with:

$$E_{KER} = \frac{p_{rel,x}^2 + p_{rel,y}^2 + p_{rel,z}^2}{2} \cdot \left(\frac{m_1 + m_2}{m_1 m_2}\right) \tag{9}$$

In typical COLTRIMS spectrometers for detecting very low energy (meV) ions from atomic ionization processes, a three dimensional focusing scheme is often used to improve the momentum resolution of the system ((27) Fig. 12). The aim of such focusing is to avoid the degrading influence of the extended reaction volume. In the direction along the spectrometer this is achieved by adding a field free drift space of twice the length of the field region following a suggestion of Wiley and McLaren (33) (or an adapted version of this idea). In directions perpendicular to the spectrometer axis, focusing can be achieved by using an electrostatic lens in the acceleration field. Such focusing can also be used for detecting the much more energetic fragments from molecular dissociation as shown by Lebech et al. (34). The disadvantage of such schemes, compared to the single field approach used here, is that higher electric fields have to be used to achieve the same collection solid angle, and the higher fields degrade the resolution on the electron side. If, as in the cases discussed here, all fragments are charged, such focusing is generally not necessary. The degrading influences of the extended source volume are reduced substantially by the evaluating relative momentum of the fragments as described above.

The typical fields in the spectrometer are in the range of 10–50 V/cm. This causes peaks from energetic fragments of

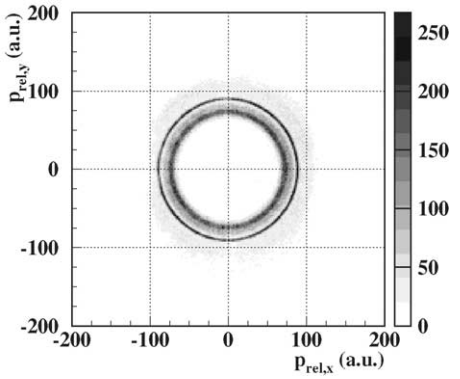

Fig. 3. Relative ion momenta of an exploding CO molecule after K-photoionization. A cut through the momentum sphere around $p_{\mathrm{rel},z} = 0$ is shown.

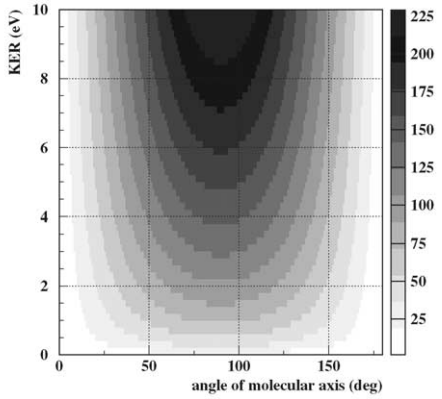

Fig. 4. Simulated resolution of the KER (eV) for different angles of the molecular axis (deg) of N_2 with respect to the spectrometer's symmetry axis. The molecule is perpendicular to that axis when the angle is 90deg. The spectrometer's parameters for the simulation are $s_r = 3$ cm, $F_r = 10$ V/cm. The assumed resolution for the time-of-flight and the position measurement are 0.5 ns and 0.5 mm, respectively. The size of the target spot is 0.5 mm/0.5 mm/0.5 mm. The gray value corresponds to the resolution (in meV).

different masses to overlap in the ion time of flight spectrum. Lighter fragments initially moving away from the detector are turned by the field toward the detector, but can overtake the heavier fragments that have initial velocities in the direction of the detector. Thus from a particle's time-of-flight, its mass cannot be determined. Instead the momentum of each of the two measured coincident ions is calculated assuming that the first arrival, ion_1, has mass $= m_1$ and the second, ion_2, has mass $= m_2$. Then, the same calculation is done with the mass assignment reversed. The combination that conserves momentum is taken as the correct assignment and is used in the further analysis. Note that, in the molecular center of mass, the heavy fragment momenta add to zero; hence, in two fragment dissociation, the momenta are equal in magnitude and opposite in direction. (This neglects the relatively small momentum transferred to the fragments by the photo electron and Auger electron emissions). Because the KER depends only on the relative momentum, effects of the center of mass motion, such as the initial thermal motion, or recoil from the Auger electron emission are removed. A typical distribution of the ions' relative momenta is shown in Fig. 3, where a cut through the momentum sphere of a Coulomb exploding CO molecule reveals several concentric, ring-like structures that correspond to the KER-distribution (see Fig. 11a)).

For a typical acceleration length of $s_r = 3$ cm and an electric field of $F_r = 10$ V/cm ionic fragments with an energy of up to $E_{\mathrm{ion}} = 9$ eV can be detected with a solid angle of 4π on a standard delayline detector (35) with a diameter of 80 mm. With a position resolution of 0.5 mm and a timing resolution of 500 ps, a resolution as shown in Fig. 4 is achieved on the KER.

3. Electron arm of the spectrometer for low energy electrons

Depending on the type of application, two different designs for the electron-side of the spectrometer have been used. When detecting electrons of low energy (up to ~ 30 eV), a standard implementation, as described in (27), can be chosen.

Since the spectrometer's electric field is already determined by the ion side, the magnetic field B and the length of the electron side s_e are the remaining parameters to be chosen. As the magnetic field is used to confine the electrons within the spectrometer's volume, the value of the field, B, depends upon the maximum electron energy, E_e, and the detector radius, r_D. The electron motion in the spectrometer consists of a cyclotron motion in the plane (x, y) perpendicular to the spectrometer's symmetry axis and fields, and an uniform acceleration followed by drift along that axis (z direction). The cyclotron radius of an electron with energy E_e:

$$r_{\mathrm{cyc}} = \frac{\sqrt{2mE_e}}{eB} \tag{10}$$

or,

$$r_{\mathrm{cyc}}\,(\mathrm{cm}) = 3.37 \cdot \frac{\sqrt{E_e\,(\mathrm{eV})}}{B\,(\mathrm{G})} \tag{11}$$

An electron's distance, r_e, at time t_e in the x, y plane from its origin at x_{orig}, y_{orig} is given by:

$$r_e = r_{\mathrm{cyc}}\sqrt{2\left(1 - \cos\left(2\pi \times \frac{t_e}{t_{\mathrm{cyc}}}\right)\right)} \tag{12}$$

where t_{cyc} is the cyclotron period,

$$t_{\mathrm{cyc}} = 2\pi\frac{m}{eB} \tag{13}$$

or,

$$t_{\mathrm{cyc}}\,(ns) = \frac{358}{B(\mathrm{G})} \tag{14}$$

Normally x_{orig}, y_{orig} is near the axis of the spectrometer, thus, to be sure that all the electrons strike the detector one must have $r_D > 2 \cdot r_{cyc}$ when the cyclotron radius is largest, i.e. when the electron's initial velocity is in the x, y plane.

Note that $r_e = 0$ when t_e is an integer multiple of t_{cyc}. At these "nodes" in the electron motion, its x and y momentum components cannot be determined. Therefore one chooses s_e such that $t_{cyc} > t_{e,max}, t_{e,min} > 0$ or $2 \cdot t_{cyc} > t_{e,max}, t_{e,min} > t_{cyc}$; where $t_{e,max}$ and $t_{e,min}$ are the maximum and minimum electron flight times. That is, the spectrometer length is such that the electron time-of-flight distribution falls within the first or second cyclotron period following the ionization.

The electron flight time, t_e is dependent upon its initial velocity component v_z along the spectrometer axis, its acceleration a_e in the uniform electric field and the length parameter, s_e. One obtains:

$$t_e = \frac{\sqrt{v_x^2 + 2s_e a_e} - v_z}{a_e} + \frac{2s_e}{\sqrt{v_x^2 + 2s_e a_e}} \tag{15}$$

where $t_{e,max}$ is obtained when the initial velocity is away from the detector, i.e. $v_z = -v_0$, and,

$$v_0 = \sqrt{\frac{2E_e}{m}}. \tag{16}$$

$t_{e,min}$ is given by the opposite case, i.e. when $v_z = v_0$. Note that the time spread of the electron distribution is given by:

$$t_{e,max} - t_{e,min} = \frac{2v_0}{a_e} \tag{17}$$

or,

$$t_{e,max} - t_{e,min}\,(\text{ns}) = 67.4\frac{\sqrt{E_e\,(\text{eV})}}{F_r\,(\text{V/cm})} \tag{18}$$

In order to determine t_{cyc} and the location of the zero electron flight time, calibration runs are made with a reduced electric field, or variable photon energies (often a combination of these are used) to produce a very broad electron time-of-flight distribution that will reveal the location of nodes in the cyclotron motion. A plot of the radius of the hit on the electron detector versus the time-of-flight then yields the so called "wiggle spectrum"; an example of one of these is shown in Fig. 5. Additional calibration data are collected using single ionization of a He target. The fixed photon energy and He ionization potential yields electrons of known and energy that are useful in calibrating the electron detector.

For a typical application with an electric field $F_r = 10$ V/cm, a magnetic field of $B = 5$ G and a length of $s_e = 5.5$ cm an electron energy resolution as shown in Fig. 6 can be achieved. In this case, the target size is assumed to be a cube of 0.5 mm/0.5 mm/0.5 mm and the detector resolution taken as 500 ps in time and 0.5 mm in position.

A main source for the error in the measured electron momentum is caused by uncertainty in the exact location of the ionization event. However, since the coincident ionic fragment momenta are measured, that location can actually be obtained by calculating the position of the ionic fragments' center of mass at the instant of ionization (x_{orig}, y_{orig}). Starting from $p_1 = -p_2$, i. e. neglecting the center of mass momentum, one obtains:

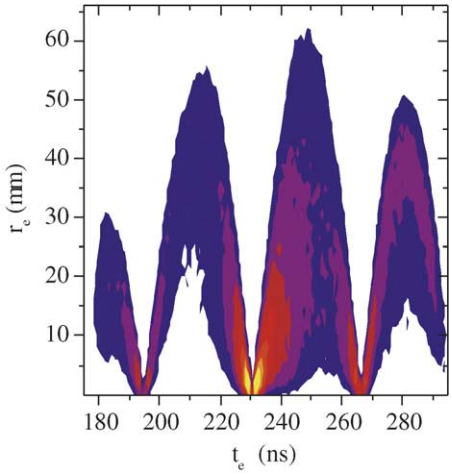

Fig. 5. The distance r_e from the spectrometer's symmetry axis versus the electron time of flight t_e showing the "nodal structure" described in the text.

$$\frac{t_2 m_1 (x_1 - x_{orig})}{t_1 t_2} = -\frac{t_1 m_2 (x_2 - x_{orig})}{t_1 t_2} \tag{19}$$

$$x_{orig} = \frac{t_2 m_1 x_1 + t_1 m_2 x_2}{t_1 m_2 + t_2 m_1} \tag{20}$$

and

$$y_{orig} = \frac{t_2 m_1 y_1 + t_1 m_2 y_2}{t_1 m_2 + t_2 m_1} \tag{21}$$

Therefore, by correcting the measured electron's position by x_{orig} and y_{orig} the influence of the target region's spread can

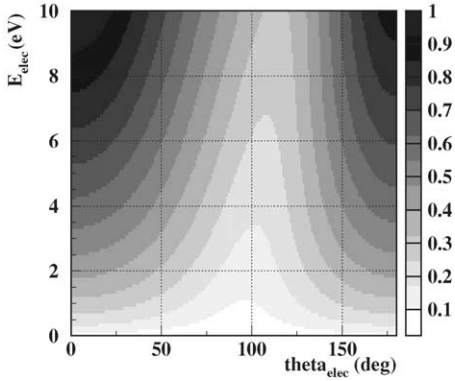

Fig. 6. Simulated resolution for a typical electron spectrometer with 4π solid angle for electrons up to 10 eV. The gray value corresponds to the energy resolution (in eV). θ_{elec} is the polar angle of electron emission with respect to the spectrometer axis, 0 deg indicates emission toward the electron detector. The spectrometer's parameters are: $s_e = 5.5$ cm, $F_r = 10$ V/cm, $B = 5$ G. The target size is assumed to be a cube of 0.5 mm/0.5 mm/0.5 mm. The detector's resolution is 500 ps in time and 0.5 mm in position.

be reduced, as shown in Fig. 7. The figure shows the energy of carbon-K photoelectrons close to threshold (16). Different vibrational levels of the ionized CO^+ molecule with a spacing of 300 meV in energy (see for example (36)) are visible. The panel on the right side is without correction for the molecule's initial CM position; the vibrational structure is less resolved than in the left panel where the correction has been applied, displaying a gain in resolution of $\sim 20\%$.

4. Electron arm of the spectrometer for high energy electrons

At electron energies substantially above 30 eV, the approach described above is no longer suitable, e.g. when dealing with molecular Auger electrons with energies of 200 eV to 500 eV. In order to achieve a satisfactory energy and angular resolution, a retarding field is implemented on the spectrometer's electron-side, as shown in Fig. 8. A part of what was the drift region is used to decelerate the high energy electrons by applying a potential of $-U_{\mathrm{ret}} = F_{\mathrm{ret}} \cdot s_{\mathrm{ret}}$ where $U_{\mathrm{ret}} = V_{\mathrm{ret}} + F_{\mathrm{r}} \cdot s_{\mathrm{e}}$. This takes into account the kinetic energy, that an electron gains inside the acceleration region, and the actual retarding voltage V_{ret}. This increases the resolution for high energy electrons, but also limits the detection to a solid angle about the spectrometer axis that is determined by the magnetic field and size of the detector. Furthermore, electrons with a momentum component p_z parallel to the symmetry axis of the spectrometer with $p_z^2/2m < V_{\mathrm{ret}} \cdot e$ will not reach the detector (see Fig. 9, area A).

As long as the ionic fragments are detected with 4π solid angle collection efficiency, complete molecular frame electron angular distributions can be obtained in spite of a limited electron solid angle. As this is the distribution of difference angles between the direction of the emitted electron and the molecular axis; fixing one of these in the laboratory (the electron direction) only limits the data collection rate. Of course, however, experiments that investigate the molecular frame electron distribution for the molecule being fixed in the laboratory frame (e.g. with respect to the polarization vector of the light) are no longer feasible, limiting that approach to either very special fixed-in-space geometries (e.g. the molecule being located within the polarization plane of circularly polarized light) or to experiments that deal with molecular frame distributions but do not have the need of fixing the molecule in the laboratory frame. Such conditions

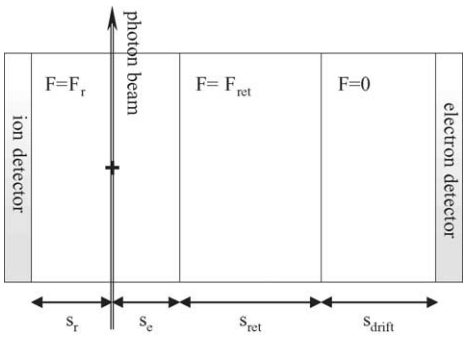

Fig. 8. A COLTRIMS spectrometer with retarding field approach for measurements of electrons with energies greater than 100 eV.

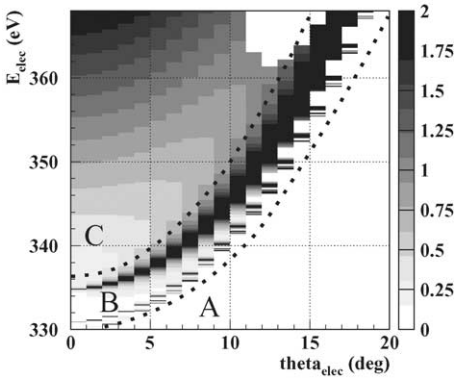

Fig. 9. Simulated resolution for a typical retarding electron spectrometer to detect electrons of 330 eV energy or higher. The detected solid angle (up to $\pm\theta_{\mathrm{e}} = 11$ deg) covered by the design varies with the energy of the electron. (θ_{e} is the polar angle of emission of the electron with respect to the direction toward the detector.) The gray value corresponds to the energy resolution (in eV). The regions A to C correspond to situations where: A, electrons are repelled by the retarding field, and therefore not detected. B, electrons with times of flight close to t_{cyc} ($B = 7$ G) causing a loss of resolution. C, Area which is actually used in the experiment.

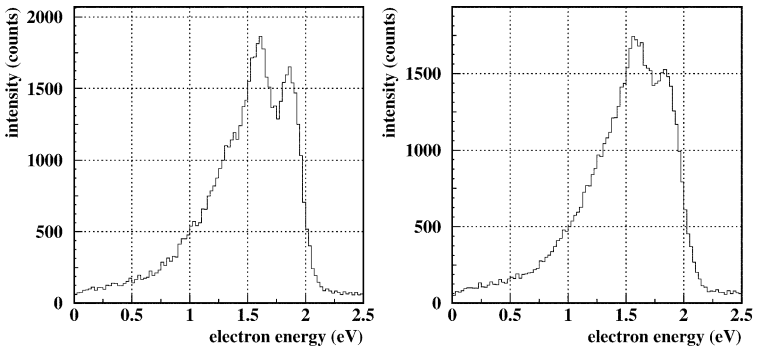

Fig. 7. Energy of C-K photoelectrons for a photon energy of 298.3 eV (16). Left: with position correction for the molecule's initial center of mass position, right: same data analyzed without this correction.

exist, for example, when Auger electrons are emitted in a two-step process (30).

These energetic electrons are detected in coincidence with molecular fragment ions whose momenta are measured as described earlier. Hence one determines the molecular KER for each event. For Auger electrons emitted from bound core-hole molecular ion states formed by photo-ionization, or from neutral core-excited molecular states, interesting insights into the molecular potential energy surfaces and decay pathways can be gained from plots of KER versus Auger electron energy. Conservation of energy yields diagonal lines with slope −1 in such plots, with a separate line corresponding to each combination of initial and final states (30). Thus placing an event on this plot can determine the decay path that produced it; an ensemble of such measurements can reveal the relative strengths of the various channels, and, selecting events that arise from one channel allows construction of its molecular frame electron angular distribution. Thus in many cases, an electron energy resolution as shown in Fig. 9 is already sufficient for very detailed investigations.

The spectrometer geometry used to investigate molecular Auger electrons after K-shell ionization of nitrogen (31) had the following parameters: the spectrometer's lengths were $s_e = 4.4\,\text{cm}$, $s_{ret} = 2.2\,\text{cm}$ and $s_{drift} = 6.6\,\text{cm}$ with a retarding potential of $V_{ret} = -330\,\text{V}$, a magnetic field $B = 7\,\text{G}$ and an electric field $E_r = 10\,\text{V/cm}$. The expected electron energy resolution (that has been verified by the experiment) is shown in Fig. 9.

5. Background suppression by coincident measurement of the molecular fragments

An additional advantage that comes with the coincident detection of the two molecular fragments (apart from improving the electron's momentum resolution, see Fig. 7) is the ability to suppress background events.

This is essential for the imaging technique to work under the typical conditions of a synchrotron radiation facility. In traditional dispersive or time-of-flight electron spectrometers great care is taken to prevent stray electrons born outside the interaction region from reaching the detector. In the case of COLTRIMS an open face channel plate without any apertures is located close to the photon beam. The typical signal rate on the electron detector under these circumstances is at least a factor of 3 above the ion count rate. In other words, at best, one of three detected electrons really originates from the investigated reaction with the target gas. Due to the multiple coincidence described here, this background does not cause any problem. A background suppression of 1 over 10^4 is easily achieved by a coincidence.

Furthermore, as valid events originate from a Coulomb exploding molecule, the back-to-back emission of the measured ionic fragments can be used as a constraint to filter out random events. If the center-of-mass momentum is negligible (usually the case for energetic fragmentation), the dependence of the second particle's time-of-flight t_2 on that of the first particle, t_1, is given by:

$$t_2 = \frac{s_r m_1}{q_2 F_r t_1} - \frac{q_1 t_1}{2q_2} + \sqrt{\frac{2 s_r m_2}{q_2 F_r} + \left(\frac{s_r m_1}{q_2 F_r t_1} - \frac{q_1 t_1}{2q_2}\right)^2} \quad (22)$$

Therefore, the distributions of the measured t_1 versus t_2 pairs yields unique curves in plots of t_2 versus t_1 for differently charged breakup channels of the molecule. Fig. 10(a) shows that distribution, commonly named "PIPICO" (photoion/photoion-coincidence)-spectrum, for the C-K ionization of carbon-monoxide. In that process curves for the case of a breakup into ion-fragment pairs C^+/O^+,C^{2+}/O^+,C^+/O^{2+} are found, that are in agreement with the prediction by Eq. (22). Therefore by selecting only those events that fall on (or near) this curve in the PIPICO spectrum, a vast amount of "background" from other channels or random events can be discarded during offline analysis.

As valid photoionization events have their origin within the region of overlap of the gas jet and the photon beam, another constraint for suppressing background can be found with Eqs. (20) and (21): only events where the calculated position of the fragments' origin falls within the interaction volume should be considered for further analysis. After applying these two constraints to the data, the histogram shown in Fig. 10(a) turns into the one shown in 10(b).

6. Examples of C and O-K-shell ionization of fixed-in-space CO

Using the non-retarding COLTRIMS spectrometer described previously, the following examples of CO photoionization have been measured, employing an electric field of $F_r = 25\,\text{V/cm}$ with a spectrometer of the dimensions $s_r = 5.5\,\text{cm}$ and $s_e = 3.9\,\text{cm}$. Fig. 11 shows the KER obtained from the measured ions' relative momenta for (a) C-K-shell ionization and (b) O-K-shell ionization of CO at photon energies of 306.4 and 553.7 eV, respectively. Several resonance-peaks are resolved as labeled in the figure according to (37). The spectra show the KER of the O^+ and C^+ fragments. These ions are created by the Auger decay of the $CO^+(1s^{-1})$ ion with the K-hole either in the O or C 1s shell, respectively. This Auger decay goes to one of the many potential energy levels of the CO^{2+} ion, which then dissociates into the measured ionic fragments. The states, that are most relevant for this problem, are shown in Fig. 12. As an example, the origin of the narrow double peak in Fig. 11(a) labeled $2^1\Sigma^+$ is shown. Here the Auger transition leads to two vibrational states in the local minimum of the second $^1\Sigma^+$ surface (sometimes called the B-state). This decays via coupling to the lowest curve shown in the diagram ($^3\Sigma^-$). The energies of all the narrow lines are determined by the CO^{2+} ion and are therefore independent of where the K-hole was. The relative intensity of the line does however change substantially, as

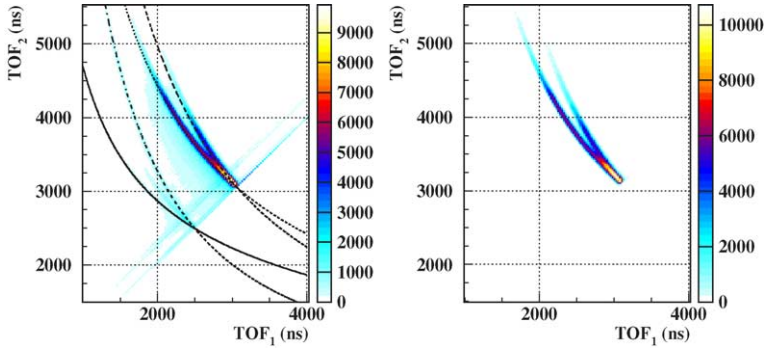

Fig. 10. PIPICO distribution for the C-K-ionization of CO. (a) Raw data with calculated relations of t_1 to t_2 according to equation 22 for the breakup channels C^{2+}/O^+, C^+/O^{2+} and C^+/O^+ (lines). (b) Same distribution after applying constraints (see text) appropriate to Coulomb explosion into C^+ and O^+ fragments.

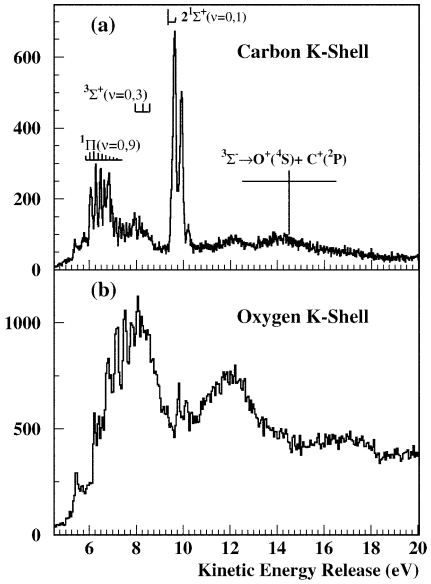

Fig. 11. Kinetic energy release of the C^+/O^+ coulomb explosion after C-K-photoionization ($h\nu = 306.4$ eV, top) and O-K-photoionization ($h\nu = 553.7$ eV, bottom).

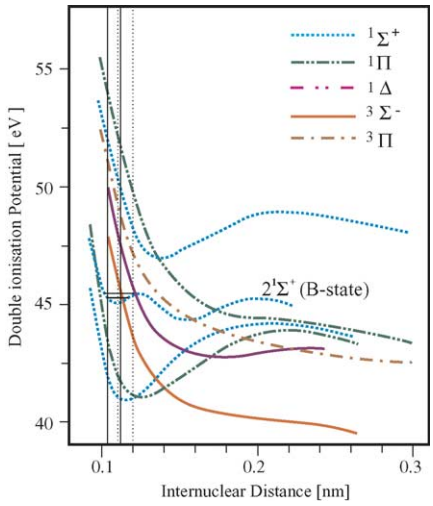

Fig. 12. Potential energy surfaces of CO^{2+} from (21). The Franck–Condon regions of $C(1s^{-1})$ and $O(1s^{-1})$ for the Auger transitions from the $CO^+(1s^{-1})$ molecule are indicated by the solid and the dotted vertical lines, respectively.

Fig. 11 strikingly illustrates. This is because the equilibrium internuclear distance of $CO^+(1s^{-1})$ is different for the O and C K-shell ionized species. The Franck–Condon region for both cases is shown in Fig. 12. For example, the well of the $2^1\Sigma^+$ is right in the middle of the Franck–Condon region of the C-K-ionized CO^+ while it is outside for the O-K-ionized CO^+. As a consequence the corresponding narrow double peak is prominent in Fig. 11(a) while it almost vanishes in Fig. 11(b). For the various broad features visible in the KER spectra the situation is different. They result from an Auger decay leading directly onto one of the steep repulsive curves in the energy level diagram. Here the position of the broad peak is determined by the position of the Franck–Condon region and hence shifts from Fig. 11(a) to (b).

Molecular frame electron angular distribution maps are shown in Fig. 13 for K-shell photoionization of CO with linearly polarized light. The angle of the molecular axis with respect to the polarization vector ε is plotted on the vertical axis, while the horizontal axis shows the electron angular

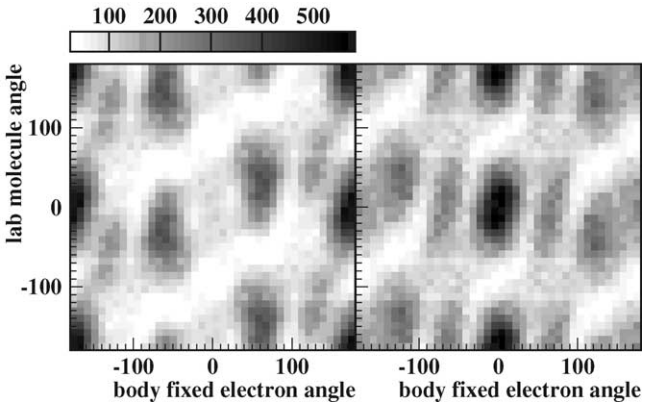

Fig. 13. Angular distribution maps of CO for a photon energy of 306.4 eV (10.2 eV above C-K threshold, left) and 553.7 eV (10.7 eV above O-K threshold, right) in comparison. The vertical axis shows the angle of the molecular axis with respect to the polarization vector of the linearly polarized light, the horizontal axis depicts the molecular frame emission angle of the photoelectron moving in the plane defined by the polarization and the molecular axis with the C atom at 0deg.

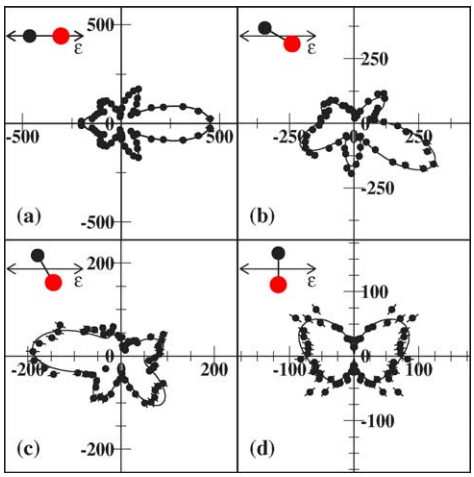

Fig. 14. Photoelectron angular distributions for selected orientations of the molecular axis with respect to the light's polarization vector (double arrow). Carbon is gray, oxygen is black. The photon energy is 306.4 eV, 10.2 eV above the C-K threshold. The solid line is a fit of spherical harmonics with up to $l = 4$.

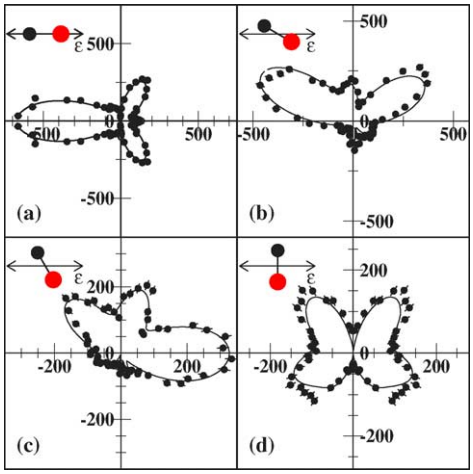

Fig. 15. Photoelectron angular distributions for a photon energy of 553.7 eV (10.7 eV above the O-K threshold for selected orientations of the molecular axis with respect to the light's polarization vector (double arrow). Carbon is gray, oxygen is black. The solid line is a fit of spherical harmonics with up to $l = 4$.

distribution in the molecular frame. Fig. 13(a) shows that map for C-K-photoionization with photons of 306.4 eV energy, Fig. 13(b) depicts the same plot for the case of O-K-photoionization (553.7 eV). While differences are only minor for the case of the molecule aligned perpendicular to the polarization vector (lab molecule angle being ±90), the electron is focused towards the O-atom in cases of C-K-ionization and towards the C-atom in the case of O-K-ionization when the molecule is aligned parallel to ε.

Photoelectron angular distributions as polar-plots for the cases of 4 different molecular alignments with respect to the polarization vector are shown in Figs. 14 and 15. The molecule's alignment is depicted by the insets at the top left of each distribution, the smaller, black circle represents the C atom. Fig. 14 shows the distributions for C-K-shell ionization, while Fig. 15 contains measured data from O-K-ionization. In all cases the solid line is a fit of spherical harmonics with l up to 4.

7. Summary

We have presented a description of many of the details of the COLTRIMS methodology as applied to recent studies of electron emission from small molecules. A description of the considerations that have to be made designing the experiment's hardware, but especially the novel possibilities of improving the experimental results when incorporating the knowledge of physical features and properties of a Coulomb exploding molecule in the offline-analysis.

On the side of extending the COLTRIMS-technique to the detection of high energy Auger electrons, the design considerations for implementing a novel retarding field method were demonstrated, including an estimation of achievable energy resolutions for an electron energy range of 330–380 eV.

Furthermore, examples for recent measurements of C- and O-K-shell photoionization of CO molecules were given. The intent was to provide the reader with insight into how these experiments are designed, and a glimpse of how one proceeds from position and time measurements to the desired momentum patterns that ultimately appear in publications that focus on the physics. The whole story is a long one beyond the scope of this piece and, to some degree, is different for every target. None-the-less the description here may be regarded as a kind of primer for the approach.

Acknowledgments

This work was supported in part by BMBF, DFG, the Chemical Sciences, Geosciences and Biosciences Division, Office of Basic Energy Sciences, Office of Science, U. S. Department of Energy.

References

[1] V. Schmidt, Rep. Prog. Phys. 55 (1992) 1483.
[2] H.C. Choi, R.M. Rao, A.G. Mihill, S. Kakar, E.D. Poliakoff, K. Wang, V. McKoy, Phys. Rev. Lett. 72 (1994) 44.
[3] A.L. Landers, Th. Weber, I. Ali, A. Cassimi, M. Hattass, O. Jagutzki, A. Nauert, T. Osipov, A. Staudte, M.H. Prior, H. Schmidt-Böcking, C.L. Cocke, R. Dörner, Phys. Rev. Lett. 87 (2001) 013002.
[4] T. Jahnke, Th. Weber, A.L. Landers, A. Knapp, S. Schössler, J. Nickles, S. Kammer, O. Jagutzki, L. Schmidt, A. Czasch, T. Osipov, E. Arenholz, A.T. Young, R. Diez Muino, D. Rolles, F.J. Garcia de Abajo, C.S. Fadley, M.A. Van Hove, S.K. Semenov, N.A. Cherepkov, J. Rösch, M.H. Prior, H. Schmidt-Böcking, C.L. Cocke, R. Dörner, Phys. Rev. Lett. 88 (2002) 073002.
[5] Y. Hikosaka, J.H.D. Eland, Phys. Chem. Chem. Phys. 20 (2000) 4663.
[6] F. Heiser, O. Geßner, J. Viefhaus, K. Wieliczek, R. Hentges, U. Becker, Phys. Rev. Lett. 79 (1997) 2435.

[7] T. Weber, O. Jagutzki, M. Hattass, A. Staudte, A. Nauert, L. Schmidt, M.H. Prior, A.L. Landers, A. Bräuning-Demian, H. Bräuning, C.L. Cocke, T. Osipov, I. Ali, R. Diez Muino, D. Rolles, F.J. Garcia de Abajo, C.S. Fadley, M.A. Van Hove, A. Cassimi, H. Schmidt-Böcking, R. Dörner, J. Phys. B34 (2001) 3669.
[8] J. Adachi, K. Hosaka, S. Furuya, K. Soejima, M. Takahashi, A. Yagishita, S.K. Semenov, N.A. Cherepkov, Phys. Rev. Lett. 91 (2003) 163001.
[9] E. Shigemasa, J. Adachi, K. Soejima, N. Watanabe, A. Yagishita, N.A. Cherepkov, Phys. Rev. Lett. 80 (1998) 1622.
[10] N. Watanabe, J. Adachi, K. Soejima, E. Shigemasa, A. Yagishita, Phys. Rev. Lett. 78 (1997) 4910.
[11] N.A. Cherepkov, S.K. Semenov, Y. Hikosaka, K. Ito, S. Motoki, A. Yagishita, Phys. Rev. Lett. 84 (2000) 250.
[12] N.A. Cherepkov, G. Raseev, J. Adachi, Y. Hikosaka, K. Ito, S. Motoki, M. Sano, K. Soejima, A. Yagishita, J. Phys. 33 (2000) 4213.
[13] K. Ito, J. Adachi, R. Hall, S. Motoki, E. Shigemasa, K. Soejima, A. Yagishita, J. Phys. 33 (2000) 572.
[14] K. Ito, J. Adachi, Y. Hikosaka, S. Motoki, K. Soejima, A. Yagishita, G. Raseev, N.A. Cherepkov, Phys. Rev. Lett. 85 (2000) 46.
[15] S. Motoki, J. Adachi, K. Ito, K. Ishii, K. Soejima, A. Yagishita, S.K. Semenov, N.A. Cherepkov, Phys. Rev. Lett. 88 (2002) 063003.
[16] T. Jahnke, L. Foucar, J. Titze, R. Wallauer, T. Osipov, E.P. Benis, A. Alnaser, O. Jagutzki, W. Arnold, S.K. Semenov, N.A. Cherepkov, L.Ph.H. Schmidt, A. Czasch, A. Staudte, M. Schöffler, C.L. Cocke, M.H. Prior, H. Schmidt-Böcking, R.Dörner, Phys. Rev. Lett., 93(2004) 083002.
[17] C.S. Fadley, Prog. Surf. Sci. 16 (1984) 245.
[18] S.H. Xu, M. Keeffe, Y. Yang, C. Chen, M. Yu, G.J. Lapeyre, E. Rotenberg, J. Denlinger, J.T. Yates, Phys. Rev. Lett. 84 (2000) 939.
[19] T. Suzuki, S. Minemoto, T. Kanai, H. Sakai, Phys. Rev. Lett. 92 (2004) 133005.
[20] T.P. Rakitzis, A.J. van den Brom, M.H.M. Janssen, Science 19 (2004) 1852.
[21] P. Lablanquie, J. Delwiche, M.-J. Hubin-Franskin, I. Nenner, P. Morin, K. Ito, J.H.D. Eland, J.-M. Robbe, G. Gandara, J. Fournier, P.G. Fournier, Phys. Rev. A 40 (1989) 5673.
[22] A.V. Golovin, F. Heiser, C.J.K. Quayle, P. Morin, M. Simon, O. Gessner, P.M. Guyon, U. Becker, Phys. Rev. Lett. 79 (1997) 4554.
[23] O. Gessner, Y. Hikosaka, B. Zimmermann, A. Hempelmann, R.R. Lucchese, JH.D. Eland, P.M. Guyon, U. Becker, Phys. Rev. 88 (2002) 193002.
[24] Y. Hikosaka, J.H.D. Eland, J. Phys. B33 (2000) 3137.
[25] T. Osipov, C.L. Cocke, M.H. Prior, T. Weber, O. Jagutzki, L. Schmidt, H. Schmidt-Böcking, R.Dörner, A. Landers, Phys. Rev. Lett., 90(2003) 233002.
[26] R.N. Zare, Mol. Photochem. 4 (1972) 1.
[27] R. Dörner, V. Mergel, O. Jagutzki, L. Spielberger, J. Ullrich, R. Moshammer, H. Schmidt-Böcking, Recoil ion momentum spectroscopy—a momentum microscope to view atomic collision dynamics, Phys. Rep. 330 (2000) 96–192.
[28] J. Ullrich, R. Moshammer, A. Dorn, R. Dörner, L.Ph.H. Schmidt, H. Schmidt-Böcking, Rep. Prog. Phys. 66 (2003) 1463–1545.
[29] R. Dörner, H. Bräuning, O. Jagutzki, V. Mergel, M. Achler, R. Moshammer, J. Feagin, A. Bräuning-Demian, L. Spielberger, J.H. McGuire, M.H. Prior, N. Berrah, J. Bozek, C.L. Cocke, H. Schmidt-Böcking, Phys. Rev. Lett. 81 (1998) 5776.
[30] Th. Weber, M. Weckenbrock, M. Balser, L. Schmidt, O. Jagutzki, W. Arnold, O. Hohn, E. Arenholz, T. Young, T. Osipov, L. Foucar, A. De Fanis, R. Diez Muino, H. Schmidt-Böcking, C.L. Cocke, M.H. Prior, R. Dörner, Phys. Rev. Lett. 90 (2003) 153003.
[31] T. Jahnke, Dissertation, Johann Wolfgang Goethe Universität Frankfurt, 2004.
[32] R. Moshammer, M. Unverzagt, W. Schmitt, J. Ullrich, H. Schmidt-Böcking, Nucl. Instrum. Meth. B108 (1996) 425.
[33] W.C. Wiley, I.H. McLaren, Rev. Sci. Instrum. 26 (1955) 1150.
[34] D. Dowek, M. Lebech, J.C. Houver, Rev. Sci. Instruments 73 (2002) 1866–1874.
[35] See http://www.Roentdek.com for details of the detectors.
[36] K.J. Randall, A.L.D. Kilcoyne, H.M. Köppe, J. Feldhaus, A.M. Bradshaw, Phys. Rev. Lett. 71 (1993) 1156.
[37] M. Lundqvist, P. Baltzer, D. Edvardsson, L. Karlsson, B. Wannberg, Phys. Rev. Lett. 75 (1995) 1058.